10

Resonant Tunnelling Optoelectronic Circuits

José Figueiredo[1], Bruno Romeira[1], Thomas Slight[2] and Charles Ironside[2]
[1]*Centro de Electrónica, Optoelectrónica e Telecomunicacões, Universidade do Algarve*
[2]*Department of Electronics and Electrical Engineering, University of Glasgow*
[1]*Portugal*
[2]*United Kingdom*

1. Introduction

Nowadays, most communication networks such as local area networks (LANs), metropolitan area networks (MANs), and wide area networks (WANs) have replaced or are about to replace coaxial cable or twisted copper wire with fiber optical cables. Light-wave communication systems comprise a transmitter based on a visible or near-infrared light source, whose carrier is modulated by the information signal to be transmitted, a transmission media such as an optical fiber, eventually utilizing in-line optical amplification, and a receiver based on a photo-detector that recovers the information signal (Liu, 1996)(Einarsson, 1996). The transmitter consists of a driver circuit along a semiconductor laser or a light emitting diode (LED). The receiver is a signal processing circuit coupled to a photo-detector such as a photodiode, an avalanche photodiode (APD), a phototransistor or a high speed photoconductor that processes the photo-detected signal and recovers the primitive information signal.

Transmitters and receivers are classical examples of optoelectronic integrated circuits (OEICs) (Wada, 1994). OEIC technologies aim to emulate CMOS microelectronics by (i) integrating optoelectronic devices and electronic circuitry on the same package or substrate (hybrid integration), (ii) monolithically integrate III-V optoelectronic devices on silicon (difficulty since silicon is not useful for many optoelectronic functions) or (iii) monolithically integrate III-V electronics with optoelectronic devices. The simply way to do hybrid integration is combining packaged devices on a ceramic substrate. More advanced techniques include flip-chip/solder-ball or -bump integration of discrete optoelectronic devices on multi-chip modules or directly on silicon integrated circuit (IC) chips, and flip-bonding on IC chips. Although, hybrid integration offers immediate solutions when many different kinds of devices need to be combined it produces OEICs with very low device density. Moreover, in certain cases the advantages of using optical devices is greatly reduced. On the contrary, monolithic integration leads to superior speed, component density, reliability, complexity, and manufacturability (Katz, 1992).

There was been substantial efforts towards monolithical integration of III-V electronics with optoelectronic devices to improve the performance of transmitters and receivers. Approaches to light modulation, light detection and light generation at microwave and millimetre-wave frequencies have been investigated by combining double barrier quantum well (DBQW) resonant tunnelling diodes (RTDs) with optical components such as

Source: Advances in Optical and Photonic Devices, Book edited by: Ki Young Kim,
ISBN 978-953-7619-76-3, pp. 352, January 2010, INTECH, Croatia, downloaded from SCIYO.COM

waveguides (Figueiredo, 2000) and semiconductor lasers (Slight, 2006). These RTD based OEICs can operate as novel optoelectronic voltage controlled oscillators (OVCOs), with potential to simplify clock recovery circuits, improve control of microwave oscillators functionalities, to generate electrical and optical aperiodic waveforms, and as microwave-to-optical subcarrier and optical subcarrier-to-microwave converters for radio-over-fiber systems, where the integration of electrical and optical components in a single chip is a major challenge in order to obtain high reliability, small size and low cost (Sauer et al., 2007).

This chapter reports investigation on resonant tunnelling (RT) based OEICs that demonstrate new functionalities for optical modulators and sources for application in telecommunication systems and signal processing circuits. Section 2 starts with a brief description of DBQW-RTD's operating principle, followed by the presentation of a physics based model of its current-voltage ($I-V$) characteristic, continues with a small-signal equivalent circuit analysis, and ends with an overview of more relevant optoelectronic devices incorporating RT structures. Section 3 describes the integration of DBQW-RTDs within an optical waveguide (OW) towards the implementation of very low driving voltage electro-absorption modulators (EAMs) and optical detectors (OD), with built-in amplifiers, for operation at optical wavelengths around 900 nm and 1550 nm. Section 4 discusses monolithic and hybrid integration of a DBQW-RTD with a laser diode (LD), its operation principle and optoelectronics circuit model used to analyse its modes of operation including optoelectronic voltage controlled oscillator (OVCO), frequency division and multiplication, phase-locking, and the generation of aperiodic, even chaotic, waveforms. The chapter ends with conclusion and acknowledgement sections.

2. Resonant tunnelling diode

Resonant tunnelling diodes (RTDs) are nanoelectronic structures that can be easily integrated with conventional electronic and photonic devices (Davies, 1998)(Mizuta & Tanoue, 1995)(Sun et al., 1998), such as transistors (Mazumder et al., 1998), optical waveguides (McMeekin et al., 1994)(Figueiredo, 2000) and laser diodes (Slight, 2006) with potential to not only reduce power consumption and cost but also increase functionality, speed and circuit reliability, without losing any advantage of using optical devices. They have two distinct features when compared with other semiconductor devices (Mazumder et al., 1998): their potential for extremely high frequency operation up to terahertz and their negative differential conductance (NDC). The former arises from the very small size of the resonant tunnelling structure along the direction of carriers transport. The second corresponds to electric gain which makes possible to operate RTDs as amplifiers and oscillators, significantly reducing the number of elements required for a given function (Mazumder et al., 1998). Functional RTD based devices and circuits span from signal generators, detectors and mixers, multi-valued logic switches, low-power amplifiers, local oscillators, frequency locking circuits, and also as generators of multiple high frequency harmonics (Mizuta & Tanoue, 1995). In this section, the physics of double barrier quantum well resonant tunnelling diodes (DBQW-RTDs) is discussed and analyzed, aiming at its application in high speed optoelectronic converters (rf-optical and optical-rf), such as light emitters, light modulators and light detectors.

2.1 Double barrier quantum well RTD

Resonant tunnelling through double potential barriers was predicted by (Bohm, 1951). Latter, (Iogansen, 1964) discussed the possibility of resonant transmission of an electron through double barriers formed in semiconductor crystals. They concluded that structures with identical barriers show tunnelling transmission coefficients of 1 when the particles incident energy equals the structure resonant energies, however small the transmission through the individual barriers may be (Mizuta & Tanoue, 1995). Figure 1 compares schematically the transmission coefficient $T(E)$ for single and symmetrical double barrier structures. The transmission coefficient lobs broadens with increasing energy because the barriers become more transparent (Davies, 1998).

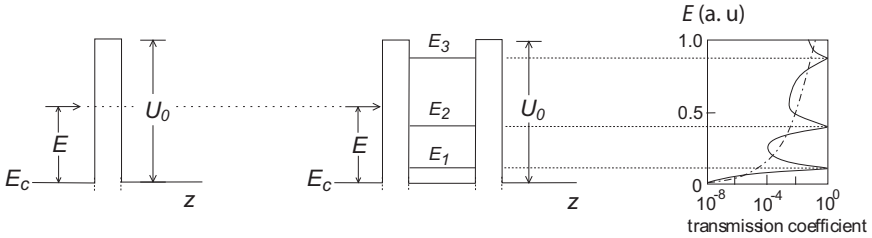

Fig. 1. Single and DBQW transmission coefficients as function of incident carrier energy.

A semiconductor double barrier quantum well resonant tunnelling diode (DBQW-RTD) consists of a low band-gap semiconductor layer (the quantum well, typical 5 nm to 10 nm wide) surrounded by two thinner layers of higher band-gap material (barriers, typical 1.5 nm to 5 nm), both sandwiched between low band-gap *n*-type material layers, typical the well material, as schematically shown in Fig. 2(a) (Mizuta & Tanoue, 1995). The material forming the barriers must have a positive conduction-band offset with respect to the smaller bandgap materials (Weisbuch & Vinter, 1991). When both sides are terminated by highly doped semiconductor layer (the emitter and the collector contacts) for electrical connection the structure is called resonant tunnelling diode (RTD). Figure 2(b) shows a schematic of a *n*-type Al-GaAs/GaAs DBQW-RTD, together with the Γ-conduction band profiles at around zero volts and at the peak voltage. Because finite height of the energy barriers the allowed energy states in the well region become quasi-bound or resonant states, Fig. 2(a), rather than true bound states as it happens with thicker barrier quantum wells (Davies, 1998). In consequence, tunneling of charge carriers through the barriers is strongly enhanced when their energy equals to one of well energy levels, reaching much higher values than the product of the two individual barrier transmission coefficients at the energy values of the system resonant levels, see Fig. 1.

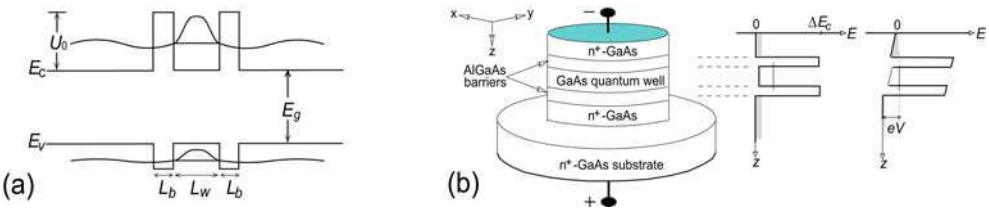

Fig. 2. (a) DBQW semiconductor structure. (b) AlGaAs DBQW structure (left); Γ-conduction band profiles at zero and at the first resonance voltage (right).

Under applied bias, the overall carrier flow through a DBQW-RTD is qualitatively different from that of a single barrier diode since the double barrier structure acts as a band filter to charge carrier energy distribution (Mizuta & Tanoue, 1995)(Sun et al., 1998). This filter action is exploited applying a voltage across the DBQW structure to control the number of carriers that can take part in the conduction through resonant levels. The carrier transmission coefficient maxima shown in Fig. 1 give rise to current-voltage characteristics with regions of strong NDC. The resonant tunnelling phenomenon in AlGaAs DBQW structures was first predicted in 1973 (Tsu & Esaki, 1973), and demonstrated experimentally in 1974 (Chang et al., 1974). In 1983, Sollner et al. demonstrated resonant tunnelling through quantum wells at frequencies up to 2.5 THz (Sollner et al., 1983). Figure 3(a) shows a typical InGaAs/AlAs RTD I –V characteristic. The main carrier flow processes in a DBQW-RTD polarized at the peak voltage (the current first maxima) is schematically represented in Fig. 3(b).

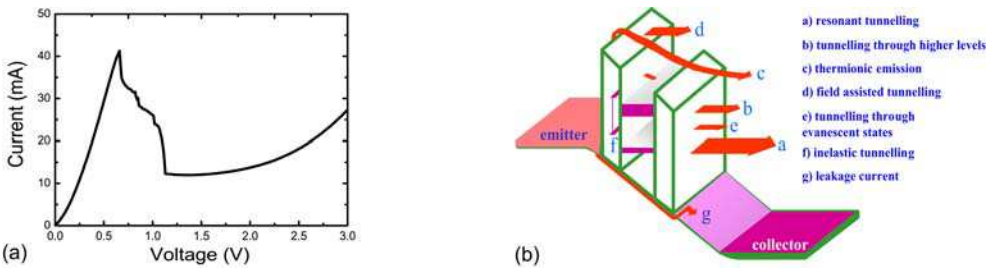

Fig. 3. (a) Typical InGaAlAs RTD I-V characteristic. (b) Current transport mechanisms in DBQW-RTDs at the peak voltage (Sun et al., 1998).

The RTD current-voltage characteristic of Fig. 3(a) can be understood with the help of the Γ-conduction band profile shown in Figs. 2(b) and 3(b) (Davies, 1998). When the applied bias is small, i.e., $V << V_p$ (peak voltage, also referred as resonance voltage), the Γ-conduction band profile is not much affected, remaining almost flat, see Fig. 2(b). The first resonant level is well above the emitter Fermi level, and little current flows. As voltage is increased, the energy of the first resonant level is moved downwards to the emitter Fermi level, leading to an almost linearly current increase with the voltage, the first positive differential conductance (PDC) region, till reaching a local maximum I_p, ideally, at $V \simeq 2E_{n=1}/e$, when the overlap between the emitter electron Fermi sea energy spectrum and the transmission coefficient around the first resonant level reaches a local maximum, as shown in the right side of Fig. 2(b) and Fig. 3(b). A further increase in the applied voltage pulls the first resonant level towards the bottom of the Γ-valley and into the forbidden gap, where there are no longer carriers available to efficiently cross the DBQW. This leads to a sharp current decrease, giving rise to the first negative differential conductance (NDC) portion of the device current-voltage characteristic. At a given voltage, known as the valley voltage V_v, with $V_v > V_p$, the current reaches a local minimum I_v. An additional increase on the bias voltage will further lift up the emitter Fermi level and tunnelling through higher resonant levels or through the top regions of the barriers will lead to new current rise, similar to the classical diode I – V characteristic (Davies, 1998). The resonant tunnelling component dominates at low voltages and the classical diode component takes over at higher voltages. For more details see (Davies, 1998)(Sun et al., 1998). In a circuit, the NDC provides the gain necessary to sustain oscillations (Mizuta & Tanoue, 1995) (Brown & Parker 1996). The

presence of a small inductance in circuit containing an RTD, together with RTD intrinsic capacitance make possible the oscillations at very high frequencies, experimental demonstrated up to 831 GHz (Suzuki et al., 2009). Frequencies never reached by other semiconductor devices: the RTD is currently the fastest purely electronic device.
The most common material systems used to implement RTD devices are III-V compounds such as AlGaAs and InP-based materials.. Si/SiGe RTDs based on Si/SiGe heterojunctions have been demonstrated but the performance is not comparable to III-V RTDs because of the limited band edge discontinuity in both valence and conduction bands. Organic RTDs are currently being investigated (Park et al., 2006)(Ryu et al., 2007)(Zheng et al., 2009).

2.2 RTD based generalized Liénard oscillator

The RTDs inherent high speed operation, up to terahertz frequency, the pronounced nonlinear current-voltage characteristic, wide-bandwidth NDC, structural simplicity, flexible design, relative ease of fabrication, and versatile circuit functionality, make them excellent candidates for nanoelectronic circuit applications. In order to take advantage of the full potential of RTD based devices several attempts have been made to incorporate the full RTD characteristics into circuit simulation packages such as SPICE-like CAD tools (Mizuta & Tanoue, 1995)(Brown et al., 1996)(Sun et al., 1998).
Since a quantum mechanics based model that includes all RTD features is not yet available, a number of empirical models have been advanced (Sun et al., 1998). Most models describe the RTD by small-signal equivalent circuits consisting of a capacitance C, resulting from charging and discharging of electrons of DBQW and depletion regions, in parallel with a voltage depend current source $I = F(V)$, a series resistance R arising mainly from the ohmic contacts and an inductance L due to bond wire connections, Fig. 4. The current source $F(V)$ is usually implemented as polynomial or piecewise functions (Brown et al., 1997)(Sun et al., 1998), which is not satisfactory if a detailed circuit description is needed. More useful RTD non-linear characteristic representations have to consider a wide variety of device structures and the materials available, i.e., the modelled $I-V$ characteristic has to be based as much as possible on the RTD physical parameters such as material properties, layer dimensions, energy levels, dopant concentrations, and the device geometry.

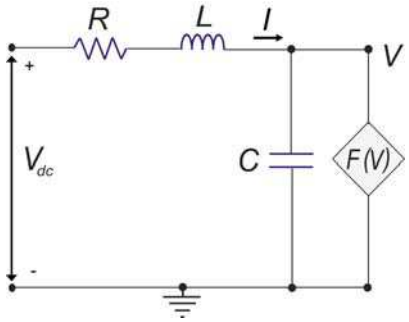

Fig. 4. Electrical equivalent circuit of an RTD represented by a capacitance in parallel with a voltage dependent current source $F(V)$. The inductance L and the resistor R are due to bonding wires and contacts.

The physics based model proposed by Schulman et al. consists of a mathematical function which provides a satisfactory $I-V$ shape characteristic for InGaAs and GaAs RTD based

devices (Schulman et al., 1996). The expression obtained contains physical quantities which can also be treated as empirical parameters for fitting purposes. In their analysis the resonant tunnelling current density is expressed within the effective mass approximation (Davies, 1998), which includes nonzero temperature, Fermi-Dirac statistics and the transmission coefficient $T(E,V)$:

$$J_{RT} = \frac{qm^* k_B T \cdot \Delta E_r}{4\pi^2 \hbar^3} \ln\left[\frac{1+e^{(E_F - E_r + qV/2)/k_B T}}{1+e^{(E_F - E_r - qV/2)/k_B T}}\right] \cdot \left[\frac{\pi}{2} + \tan^{-1}\left(\frac{E_r - qV/2}{\Delta E_r/2}\right)\right] \quad (1)$$

where $E = E_r - qV/2$ is the energy measured up from the emitter conduction band edge, E_r is the energy of the resonant level relative to the bottom of the well at its centre, and ΔE_r is the resonance width. The parameters q and k_B are unit electric charge and Boltzmann constants, respectively. Equation 1 can be rewritten as:

$$J_{RT}(V) = A \cdot \ln\left[\frac{1+e^{q(B-C+n_1 V)/k_B T}}{1+e^{q(B-C-n_1 V)/k_B T}}\right] \cdot \left[\frac{\pi}{2} + \tan^{-1}\left(\frac{C-n_1 V}{D}\right)\right] \quad (2)$$

where the parameters A, B, C, D, and n_1 can be used to shape the curve to match the first PDC region of the measured $I-V$ characteristic, having at the same time a well-defined physical interpretation: A and B are related, among other factors, with resonance width and Fermi level energies, and allow adjustment of the RTD peak current; C and n_1 determine essentially the RTD peak voltage, correlated with the energy of the resonant level relative to the bottom of the well and with the transmission coefficient; finally, D is related to the resonance width ΔE_r.

In order to represent the increasing valley current due to tunnelling through higher resonances or thermal excitation over the barriers, an additional current density component, identical to the classical diode current, the non-resonant term J_{NR}, have to be included:

$$J_{NR}(V) = H\left(e^{n_2 qV/k_B T} - 1\right) \quad (3)$$

Parameters D and H adjustment of adjust the peak to valley current ratio (PVCR) and the peak to valley voltage ratio (PVVR).

Equations 2 and 3 give good estimations of the peak current and the NDC region of current-voltage characteristic. The final form of the RTD current-voltage curve is then given by:

$$I(V) = I_{RT}(V) + I_{NR}(V) = M[J_{RT}(V) + J_{NR}(V)] \quad (4)$$

where the multiplying factor M is used to scale equation 4, in order to take into account the devices area. Figure 5 shows experimental $I-V$ curves of AlGaAs (a), and InGaAlAs (b), RTDs, with the corresponding fit given by equation 4. The fits assumed operation at temperature T =300 K and a multiplying factor M=2×10^{-6} cm^2, with the following parameters: A=1950 A/cm^2, B=0.05 V, C=0.0874 V, D=0.0073 V, n_1=0.0352, H=18343 A/cm^2, and n_2=0.0031 for AlGaAs; A=3800 A/cm^2, B=0.068 V, C=0.1035 V, D=0.0088 V, n_1=0.0862, H=4515 A/cm^2, and n_2=0.0127 for InGaAlAs. Higher values of A and B are used in the InGaAlAs fitting due to RTD higher peak current; parameter D was also slightly larger for the InGaAlAs due to superior PVCR and PVVR. The parameter H was around four times larger in the AlGaAs due mainly to their higher peak voltages.

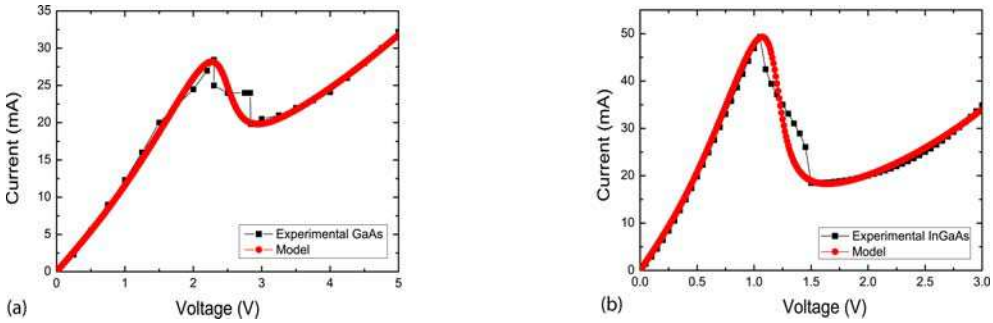

Fig. 5. GaAs/AlAs (a) and InGaAs/AlAs (b) RTD experimental I –Vs and fittings.

Since the RTD is a voltage-dependent current source device, when incorporated in a resonant circuit and biased in the NDC portion of its I –V characteristic produces oscillations at circuit characteristic frequency (Brown & Parker, 1996). In order to understand the origin of the circuit self-oscillations induced by the RTD we consider the small-signal equivalent circuit of Fig. 4. Typical RTD switching times are in general dominated by the effects of current densities and capacitances, i.e., by the circuit RC time constant (Brown et al., 1997) (Brown & Parker, 1996).

A general analysis of a circuit containing an RTD considers the small signal equivalent circuit of Fig. 4, where the RTD non-linear I –V characteristic is represented by a voltage dependent current source $F(V)$, given by equation 4, in parallel with RTD intrinsic capacitance C. Resistor R and inductor L encompasses for the device series resistance and connections inductance, respectively. By applying Kirchoff's laws (using Faraday's law) to the circuit of Fig. 4, the voltage V across the capacitance C and the current I through the inductor L are given by the following set of two first-order non-autonomous differential equations (Slight et al., 2008):

$$\dot{V} = \frac{1}{C}\left[I - F(V)\right] \tag{5}$$

$$\dot{I} = \frac{1}{L}\left(V_{dc} - RI - V\right) \tag{6}$$

After some algebra, we find that the system of Eqs. 5-6 is equivalent to the following second-order differential equation, referred as one of the generalized nonlinear Liénard systems (Slight et al., 2008)(Figueiredo, 1970):

$$\ddot{V} + \left[\frac{R}{L} + \frac{1}{C}\frac{dF(V)}{dV}\right]\dot{V} + \frac{1}{LC}\left[V - V_{dc} + RF(V)\right] = 0 \tag{7}$$

$$\ddot{V} + H(V)\dot{V} + G(V) = 0 \tag{8}$$

"where $H(V) = \frac{R}{L} + \frac{1}{C}\frac{dF(V)}{dV}$ and $G(V) = \frac{1}{LC}\left[V - V_{dc} + RF(V)\right]$. $G(V)$ is a nonlinear force and $H(V)\dot{V}$ is a damping factor.

The circuit of Fig. 4 dc biased in the NDC acts as a relaxation oscillator producing oscillations at a frequency around $f_0(V) \approx \left(2\pi\sqrt{L \cdot C(V)}\right)^{-1}$, the circuit characteristic frequency, whenever the series R is smaller than the RTD operating point negative differential resistance (Brown & Parker, 1996). From the application point of view the wideband NDC of RTD leads to low frequency oscillations instabilities that are detrimental. A most common source of instability arises from the dc source circuitry by introducing in the circuit an equivalent inductance, which together with RTD capacitance leads to oscillations at around few megahertz (Figueiredo, 2000)(Slight, 2006). A method to eliminate these low frequency oscillations and allowing circuit operation at much higher frequency is to place a shunt capacitor across the terminals of the device (Kidner et al., 1990)(Huang et al., 1997). The inductance is now only due to the connection from the shunt capacitor to the RTD.

2.3 Optoelectronic applications of RT structures

Several optoelectronic devices and circuits whose functions depend on embedded resonant tunnelling structures have been proposed and demonstrated, including resonant tunneling light emitting diodes (RT-LEDs) (Van Hoof et al., 1992), vertically integrated semiconductor lasers with RTDs (Grave et al., 1991), resonant tunnelling effect quantum-well lasers (Kawamura et al., 1994), resonant tunnelling injection laser (Capasso et al., 1986), multi-quantum well (MQW) lasers (Kawamura et al., 1987) and photo-detecting (PD) structures (Chen et al., 1991). The nature and the energies involved in the carrier transition induced by the light interaction with the tunnelling layers determine the operation in the optical or in the infrared part of the electromagnetic spectrum. Optical applications such as photo-detection, light emission, optical switching, utilize inter-band transitions (band-gap transitions), whereas infrared applications include intra-band and inter-sub-band photo-detection, and infrared emission. Below is presented a brief summary of the main progress on optical and optoelectronic devices whose functionalities depend of embedded RT structures.

Bistability in the light output of bipolar RT-LEDs has been reported, showing that these devices are capable of ultrafast optical switching and high frequency optical oscillation (Van Hoof et al., 1993). Laser transistors incorporating a resonant tunnelling structure have been reported, with carrier injection or extraction controlled via resonant tunnelling structure, with light output controlled by the collector voltage and achieving higher speed than with conventional semiconductor lasers (Kawamura et al., 1992). Embedding RTs into multi-quantum well (MQW) devices introduces negative differential conductance over wide valley region, which is very effective for getting large voltage switching and high on/off ratio current switching (Kawamura et al., 1988) leading to electro-optic bistability (Chen et al., 1991). Optical bistability in QW lasers integrated with DBQW-RTDs, and a RTD with a MQW modulator/detector based on the p – i(MQW)–n configuration, operating at room temperature, were reported (Kawamura et al., 1994). Clear negative differential conductance and bistability, with high contrast and high sensitivity in resonant tunnelling triangular barrier optoelectronic switch (R-TOPS), which consists of a double barrier resonant tunnelling diode and a triangular barrier phototransistor has been demonstrated (Sakata et al., 1995).

A light pulse incident upon a resonant tunnelling diode produces photo-charges that reduce the series resistance, leading to a shift of the peak and valley voltages which can induce RTD

switching and give rise to changes in the current flow (Moise et al., 1995). Optically switched resonant tunnelling diode (ORTD) photo-detectors have been demonstrated (Moise et al., 1997). Phase locking of an oscillating GaAs/AlGaAs RTD to a train of light pulses achieved by direct illumination was reported (Lann et al., 1993), as well as optical switching in resonant tunnelling diode (England et al., 1991) and optical injection locking of the resonant tunnelling oscillator (Kan et al., 2001). The RT structures can be used to implement light-by-light switching (England et al., 1991). Ultra-fast optoelectronic circuits using RTDs and uni-travelling-carrier photodiodes (UTC-PDs) to de-multiplex ultra-fast optical data signals into electrical data signals with lower bit rate and low power consumption has been demonstrated (Sano et al., 1998).
Our work on optoelectronic devices based on the integration of a RTD within an optical waveguide, and on hybrid and monolithic integrations of RTDs with laser diodes is discussed in the remaining sections of this chapter.

3. RTD optical waveguide modulator-photodetector

Novel information and communication technologies relying on microwave/millimetre-wavelightwave interactions are fundamental to the development of applications such as low-cost fibre-optic communication networks, cable television signal distribution, mobile communications, and radio local area networks (Sauer et al., 2007). In this section, electrical active, high speed, highly efficient and low-cost electro-absorption modulators and photo-detectors based on the integration of a RT structure within a semiconductor optical waveguide are described.

3.1 RTD optical waveguide integration

As discussed previously, when the RTD is biased in the valley region most of the applied voltage is dropped across the depletion region formed between the second barrier and the collector contact, Fig. 6(a), where a strong electric field builds-in. Inter-band electro-absorption of light with photon energies close to but smaller than the collector band-gap energy is achieved through the Franz-Keldysh effect (Chuang, 1995). According to the Franz-Keldysh effect the semiconductor material optical absorption band-edge is broadened by the presence of an electric field, resulting in an increase of absorption of light with photon energies smaller but close to the material band-gap (Keldysh, 1958). This effect is used to implement either electro-absorption (EAM) (intensity) modulators (Wakita et al., 1998) or waveguide photo-detectors (Chuang, 1995). However, in typical RTD structures the light is injected perpendicularly to the tunnelling plane, which gives a light interaction (absorption) length well below 100 nm, and thus very small light absorption. This limitation can be easily overcome embedding the RTD into the core of a unipolar semiconductor optical waveguide (McMeekin et al., 1994). A typical waveguide structure is represented schematically in Fig. 6(a), showing also wafer Γ-conduction band-edge and refractive index profiles. This optoelectronic device is called resonant tunnelling diode optical waveguide (RTD-OW). The waveguide refractive index distribution confines light end-fire coupled along the tunnelling layers and the collector depleted region, therefore increasing substantially the light interaction volume along the waveguide length as indicated in Fig. 6(b).
The RTD-OW, apart from the light confining layers (the lower refractive index regions – upper and lower cladding layers), corresponds to a DBQW-RTD with thick low doped

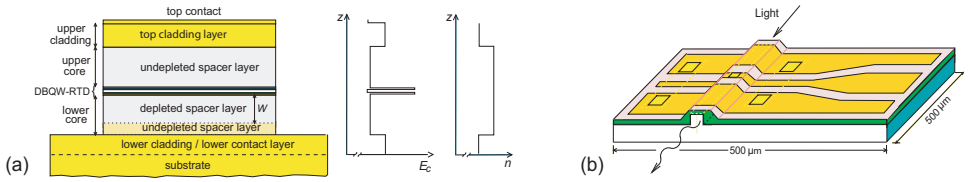

Fig. 6. (a) Diagram of a unipolar resonant tunnelling diode optical waveguide (RTD-OW) wafer structure, and the corresponding Γ-conduction band-edge and refractive index profiles. (b) Ridged waveguide channel configuration.

emitter and collector spacer layers. The presence of the DBQW within the waveguide core modifies the unipolar waveguide linear current-voltage characteristic towards the DBQW-RTD strong nonlinear I –V curve (McMeekin et al., 1994)(Figueiredo, 2000). Moreover, it leads to a non-linear electric field distribution across the collector side waveguide core that is strongly dependent on the bias voltage, due to the electron accumulation close to the emitter barrier and the creation of a depletion region on the collector spacer layer. Since a small voltage can be used to make a RTD operating point to switch between peak and valley regions, the RTD-OW can be employed to implement electro-absorption modulators (McMeekin et al., 1994)(Figueiredo, 2000). A small voltage change results in large modulation of the electric field across the device collector depletion region, resulting, though the Franz-Keldysh effect, in waveguide propagation losses and electro-absorption for photon energies close to but smaller than the waveguide core band-gap energy (Figueiredo, 2000)(Figueiredo et al., 2001).

The RTD-OW electric field distribution dependence on the bias voltage can be understood by considering the Γ-conduction band profile of the collector spacer layer, Fig. 7. Below resonance (first PDC region), the applied voltage is dropped mainly across the DBQW, and the electric field in the collector core is rather small, Fig. 7(a). Any optical loss increase with the applied voltage is mainly due to the thermal effects induced by the current flow, which rise linearly with the current. Above resonance (in the NDC and on the second PDC region), the additional applied bias voltage is dropped mainly across the depleted part of the collector spacer layer, Fig. 7(b), and the electric field magnitude is now much stronger than on the first PDC region, inducing large light absorption. The thermal optical absorption is now much less important because the current flowing through the devices biased on the valley region is significantly lower.

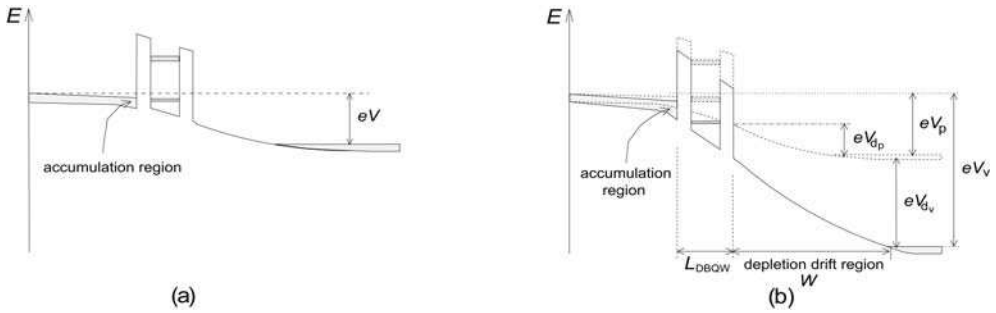

Fig. 7. Effect of applied biased on RTD-OW Γ-band: (a) before the peak and (b) on the valley.

The electric field enhancement ΔE_{VP} induced by the peak to valley switching can be estimated as (Figueiredo, 2000)(Figueiredo et al., 2001):

$$\Delta E_{VP} \simeq \Delta V_{VP} / W_{dep} + (W_{dep} / 2\varepsilon \upsilon_{sat})\Delta J_{PV} \tag{9}$$

where ΔV_{VP} is the voltage dropped across the depletion region, ΔJ_{PV} is the corresponding current density change, υ_{sat} is the carrier saturation velocity and W_{dep} is the depletion thickness. At a given photon energy the absorption change induced by the electric field enhancement due to the peak to valley switching is given by (Figueiredo, 2000):

$$\Delta\alpha(\hbar\omega, \Delta E_{VP}) = \alpha(\hbar\omega, E_V) - \alpha(\hbar\omega, E_P) \approx \alpha(\hbar\omega, \Delta E_{VP}) \tag{10}$$

where $\alpha(\hbar\omega,E)$ is given, in the weak field approximation, by the Franz-Keldysh effect electroabsorption coefficient (Chuang, 1995)(Keldysh, 1958). The light modulation depth due to the peak to valley switching can be calculated using (Chuang, 1995):

$$R_{VP}(\text{dB}) \approx 4.343\gamma_f \Delta\alpha(\hbar\omega, \Delta E_{VP})\ell \tag{11}$$

where γ_f is the optical filling factor which corresponds to the fraction of the optical power guided in the depleted region of the waveguide, and ℓ is the RTD-OW electrically active length, defined by the RTD metal contacts length [see Fig. 6(b)]. The measured Franz-Keldysh effect effective band-edge shift to longer wavelengths can be compared with the value given by theory (Chuang, 1995)(Keldysh, 1958):

$$\Delta\lambda_g \simeq (\lambda_g^2 / hc)(e^2h^2 / 8\pi^2 m_r)^{1/3} \Delta E_{VP}^{2/3} \tag{12}$$

The measured $\Delta\lambda_g$ gives an independent way to determine the electric field change ΔE_{VP} induced by the peak to valley switching.

As mentioned, RTD-OWs designed to show considerable NDC with a significant portion of the waveguide core being depleted at bias voltages higher than the peak voltage can have their operation point switched between the two I –V PDC regions by small high frequency ac signals (< 1 V). This leads to high speed electric field switching, resulting in high frequency modulation of the waveguide optical transmission loss. In this mode of operation the RTD-OW is called a resonant tunnelling diode electro-absorption modulator (RTD-EAM). In the RTD-EAM the modulation depth depends essentially on the overlap between the electric field in the collector depleted volume and the optical mode. The peak to valley electric field magnitude boost is determined mainly by the NDC region characteristics, ΔV and ΔJ. Figure 8 represents schematically the light absorption on the collector depleted region induced by the Franz-Keldysh effect when the RTD-OW is biased on the valley region, Fig. 8(a), and the change in the absorption coefficient associated with the bistable switching of the device plotted against wavelength, Fig. 8(b).

The device concept was implemented using AlGaAs ternary material system for operation on 900 nm optical window, and InGaAlAs quaternary compound to work on 1300 nm and 1550 nm optical windows, where the optical fibre present zero dispersion and have the lowest losses, respectively. For operation in the 900 nm spectral region, GaAs was used to form the waveguide core and the quantum well; AlAs and AlGaAs were employed to form the barriers and waveguide cladding layers, respectively. For operation at around 1550 nm,

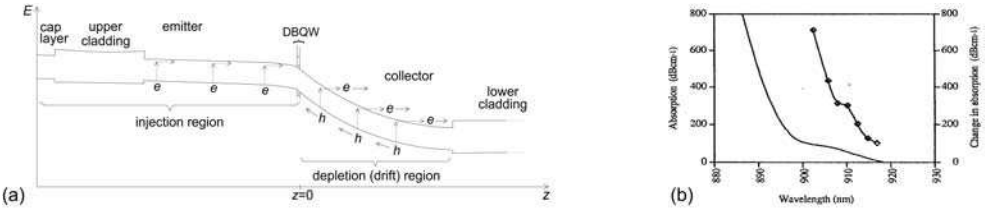

Fig. 8. (a) Schematic diagram of light absorption induced by Franz-Keldysh effect in a RTD-OW biased around the valley point. (b) Change in absorption produced by the change in the voltage characteristic of the NDC pulse plotted with the absorption in dB/cm of bulk GaAs against wavelength (McMeekin et al., 1994).

the InGaAlAs quaternary material system was used to implement the waveguide core and the quantum well, with AlAs and $In_{0.48}Al_{0.52}As$/InP being employed for the barriers and the waveguide cladding layers, respectively. The InGaAsP quaternary compound also allows operation on 1300 nm and 1550 nm optical windows but was not used. A detailed description of the RTD-OW structures implemented can be found in (Figueiredo, 2000). Next we describe the experimental operation of RTD-OW electro-absorption modulators on the optical communication windows around 900 nm and 1550 nm.

3.2 RTD-OW operation as EAM at 900 nm

The RTD-OW operation as an electro-absorption modulator at around 900 nm was achieved by growing the waveguide and DBQW layers using the AlGaAs/GaAs material system on semi-insulating GaAs. The GaAs waveguide core was made 1μm thick to allow easy end-fire light coupling, with *n*-type Si doping concentration of 2×10^{16} cm^{-3}; the cladding layers were made of $Al_{0.33}Ga_{0.67}As$, a direct band-gap compound alloy, with Si doping concentration around 2×10^{18} cm^{-3}. The refractive index difference between the core and cladding layers around 0.224 at 900 nm is sufficiently to obtain efficient light confinement with relatively thin cladding layers. The upper cladding layer thickness was made 300 nm thick, twice the reciprocal of the optical waveguide first mode exponential decaying factor, to keep the device series resistance low. Because the waveguide core and the substrate have similar real refractive indices, the lower cladding layer was made 600 nm thick with Si doping concentration of 2×10^{18} cm^{-3}, to act as an isolation layer separating the core from the substrate, in order to significantly reduce radiation leakage into the GaAs substrate. The DBQW consisted of a 7 nm GaAs quantum well sandwiched between 1.4 nm AlAs barriers. The detailed description and fabrication of AlGaAs/GaAs structures can be found in (Figueiredo, 2000). Figure 9 shows the top view of a RTD-OW die and a packaged device.

When dc biased in the NDC region, all tested devices showed instabilities at around few MHz. These where removed connecting devices to the dc power supply via a wide bandwidth bias-T. In certain cases, a high frequency energy-storage element, such as a coax transmission line, was inserted between the RTD and the bias-T, resulting in a RTD-EAM transmission line relaxation oscillator whenever the cavity characteristic frequency was within the NDC bandwidth (Figueiredo et al., 1999). Typical electrical relaxation oscillations due to a 15 cm long coaxial transmission line are shown in Fig. 10(a). The relaxation oscillations RF spectra show harmonic components up to 15 GHz (Figueiredo, 2000). The free-running oscillation frequency was changeable by varying the optical power coupled

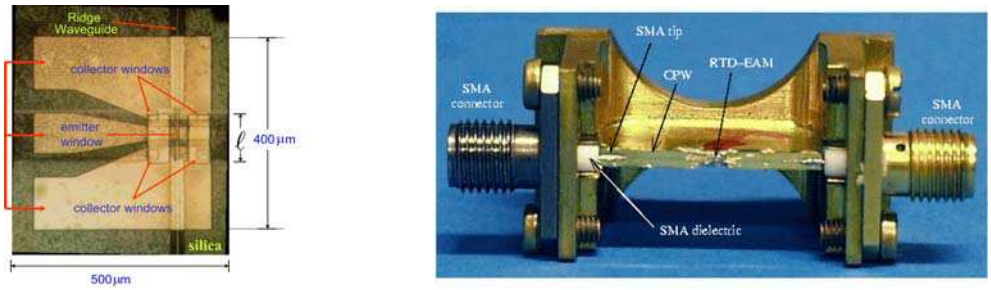

Fig. 9. RTD-OW die top view and a packaged device. The parameter ℓ here represents devices electrical active length, which with the waveguide width defines devices active area.

into the RTD-EAM, as shown in Fig. 10(b); in the cases observed the free-running frequency decreased when the coupled optical power was increased. In a circuit with a free-running oscillation frequency around 470 MHz, a tuning range of 10 MHz was observed. The frequency tuning effect is mainly due to the creation of charge carriers in the depletion region that reduces the device series resistance and moves the operating point through the NDC region, which change the device impedance [mainly the capacitance and the negative differential resistance (NDR)]. In the experiment light from a tunable Ti:sapphire laser emitting at around 900 nm was used; the optical power was kept to few mW in order to avoid damaging waveguide input facet.

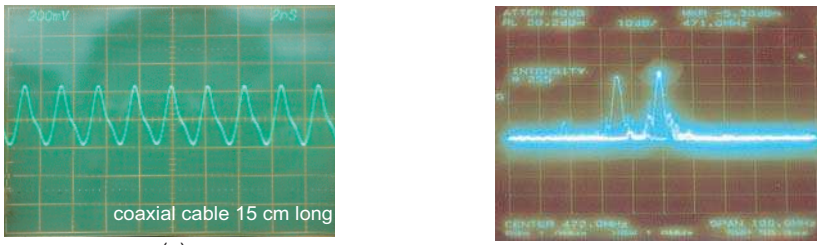

Fig. 10. (a) Self-sustained oscillations in a RTD-EAM connected via a 15 cm long coaxial line. (b) Self-oscillations frequency tuning induced by incident light.

The free-running relaxation oscillation frequency is also affected by the dc bias voltage because of the device intrinsic impedance dependence on the voltage. These behaviours can be used to implement both optical controlled oscillators (OCOs) and voltage controlled oscillators (VCOs). The OCO can be used to optically control microwave oscillators, and will be briefly analyzed when discussing the RTD-OW operation as photo-detector. The VCO behaviour makes possible operating the RTD-EAM as an optoelectronic voltage controlled oscillator (OVCO) since the electric field across the depleted collector region also self-oscillates at the free-running frequency, self-modulating the transmission properties of the waveguide. Before discussing OVCO operation we present electro-absorption response of the RTD-EAM. The RTD-EAM waveguide transmission spectra at zero bias, at slightly below the peak, and just above the valley points, are shown in Fig. 11(a) for devices with active areas around 800 μm^2. (The devices were not dc biased in the NDC region in order to avoid self-oscillation.) As the applied voltage increases from the peak to the valley point,

there is a sharp drop in the waveguide transmission at wavelengths in the range 890 nm to 910 nm. The observed Franz-Keldysh absorption band-edge shift was around 12 nm which compares to 9 nm estimated using equation 12, taking in consideration the approximations made (Figueiredo, 2000). Figure 11(b) presents the optical modulation depth as a function of the operating wavelength due to the transition between the two positive PDC regions induced by a square signal with peak-to-peak voltage slight higher than $\Delta V_{VP} = V_V - V_P$. Modulation depth up to 13 dB around 908 nm was achieved. Modulation depths up to 18 dB were observed in waveguides with 400 μm active length and 4 μm wide ridges.

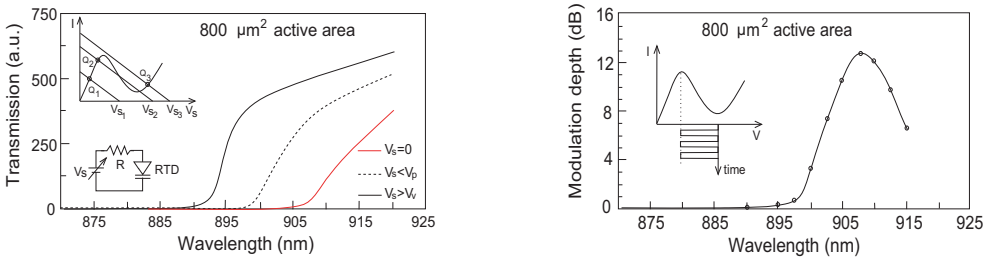

Fig. 11. (a) AlGaAs RTD-EAM optical transmission spectrum at zero volts, around the peak and at the valley region. (b) Modulation depth as function of the operating wavelength due to peak-to-valley switching induced by a square voltage waveform.

Direct modulation was obtained dc biasing the RTD-EAM slightly above the valley point and injecting through a wide band bias-T the rf modulating signals. Figure 12 shows examples of modulation due to 950 MHz and 16 GHz rf signal voltages. In both cases the driving signals amplitude was kept slightly larger than $\Delta V_{VP} \sim 0.4$ V. Optical modulation depths as high as 11 dB were achieved (Figueiredo et al., 1999)(Figueiredo, 2000). The 16 GHz response shown in Fig. 12(b) gives a good estimation of the bandwidth and modulation depth potential of the devices. The modulation efficiency characterized by the bandwidth-to-drive-voltage ratio, defined as the ratio of the operation bandwidth to the operating voltage for at least 10 dB modulation depth, was 40 GHz/V (Figueiredo et al., 1999)(Figueiredo, 2000).

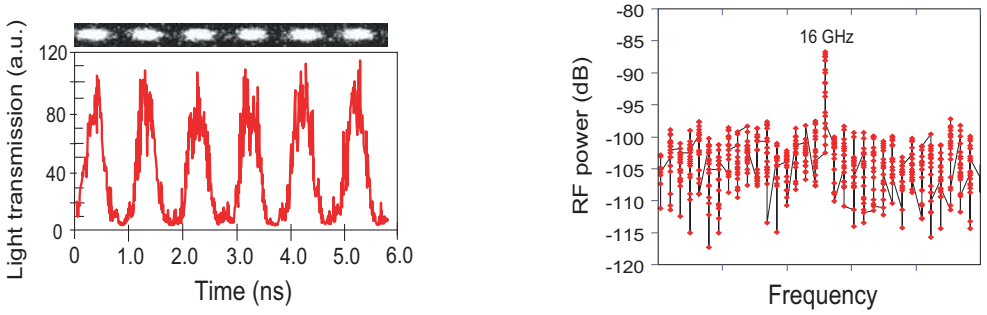

Fig. 12. (a) Direct modulation at around 950 MHz, with modulation depth up to 11 dB (λ=908 nm). (b) Modulator response to a 16 GHz rf signal.

As discussed previously, when dc biased in the NDC region and connected to a bias-T through a coaxial line the RTD-EAM can operate in the self-oscillation mode, producing an optical output modulated by the NDC induced relaxation oscillations, at frequencies determined by the electrical length of the transmission line, as shown in Fig. 13.

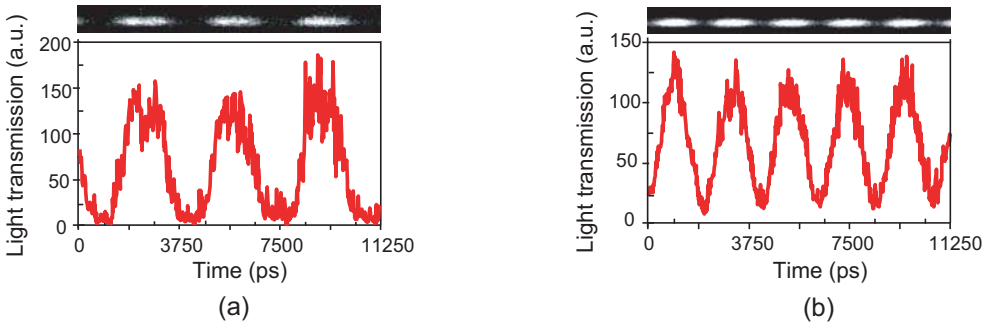

Fig. 13. Optical responses measured with Streak Camera of RTD-EAM transmission line relaxation oscillators with lines 15 cm (a) and 10 cm (b) long.

The AlGaAs RTD-EAM operation modes discussed above can be employed in LANs systems primarily as devices for electrically controlling guided-wave optical signals in the 880 nm to 1100 nm wavelength range such as waveguide intensity modulators, directional couplers and optical switches. The capability to operate in relaxation oscillation mode can be applied in clock extraction circuits, for optical pulse generation and de-multiplexing in optical time division multiplexed systems.

3.3 RTD-OW operation as EAM at 1550 nm

The AlGaAs/GaAs RTD-EAM achieved performances led the work to the demonstration of device concept operation at 1550 nm, where standard single-mode optical fibres have lowest losses (Liu, 1996). For band gap energies between 0.75 eV and 1.439 eV, quaternary alloys lattice matched to InP, which combine In, Ga, Al, and As ($In_{1-x-y}Ga_xAl_yAs$) or In, Ga, As, and P ($In_{1-x-y}Ga_xAs_{1-y}P_y$), can be used (Chuang, 1995)(Figueiredo, 2000). The RTD-OW concept operating at 1550 nm was demonstrated using InGaAlAs lattice matched to InP because phosphorus based heterostructures have lower conduction band discontinuity, which prevents strong localization of electrons in the lower band gap material. Moreover, they are difficult to grow with conventional MBE systems due to the need to handle solid phosphorus and high concentration of phosphorus at its vapour pressure, and also due to the difficulty to control As/P ratio.[1] The InGaAlAs material system shows more favorable material properties such as higher electron mobility, lower effective mass and superior conduction bandedge discontinuity (Figueiredo, 2000). As a consequence it is expected the InGaAlAs RTD-OW shows superior speed and modulation depth performance mainly to the InGaAs RTD higher peak current density and peak-to-valley current ratio, and smaller operating voltage. The In- GaAlAs quaternary system lattice matched to InP allows as well operation at 1300 nm, where standard single-mode optical fibres show zero dispersion (Chuang, 1995)(Figueiredo, 2000).

[1] Structures incorporating InGaAsP are usually grown by MOCVD (Bohrer et al., 1993).

The InGaAlAs RTD-OW schematic wafer structure for operation at 1550 nm is shown in Fig. 14, with wafer Γ-valley and refractive index profiles. The core consisted of two $In_{0.53}Ga_{0.42}Al_{0.05}As$ layers (refractive index of 3.56), 0.5 μm thick each, with a band-gap energy around 0.826 eV (absorption band-edge wavelength around 1500 nm), to allow operation at 1550 nm when biased around the peak voltage. The upper cladding was implemented using a layer of $In_{0.52}Al_{0.48}As$, refractive index of 3.24. Because InP refractive index at 1550 nm (3.17) is considerably smaller than the $In_{0.53}Ga_{0.42}Al_{0.05}As$ refractive index, the *n*-type InP substrate acted as lower cladding region. As previously discussed, the upper cladding layer thickness was made 300 nm thick. A detailed description of the wafer structure is given in (Figueiredo, 2000). Most of the RTD-EAMs characterized were 4 μm wide ridges with 200 μm active lengths. Typical current-voltage characteristic of 4 μm × 200 μm InGaAlAs/InP RTD-EAM is presented in Fig. 5(b) (section 2), showing PVCR around 3. These devices showed valley-to-peak voltage differences ΔV_{VP} ~ 0.8 V, with peak-to-valley current density differences ΔJ_{PV} ~ 10 kA/cm². (Typical GaAs/AlAs devices show ΔV_{VP} ~ 0.4 V and ΔJ_{PV} ~ 5 kA/cm².)

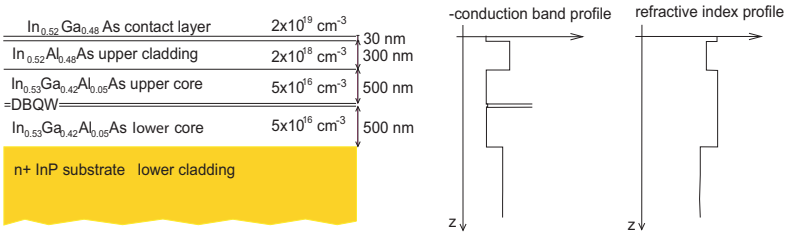

Fig. 14. InGaAlAs RTD-EAM structure, Γ-valley and refractive index profiles.

The devices' frequency response was investigated by on wafer impedance measurements in the 45 MHz to 18 GHz frequency range for all values of bias voltage. The results indicate the InGaAlAs RTD-EAM small signal equivalent circuit consists of a capacitance *C* in parallel with a non-linear resistor $R_d(V)$, in series with a resistance R_S; the series inductance was found to be negligible (Figueiredo, 2000)(Alkeev et al., 2000). The devices average capacitance *C* and shunt resistance *R* around the NDC region were 1 pF and -15 Ω, respectively; the R_S was typical few ohms (less than 5 Ω) ((Figueiredo, 2000)(Alkeev et al., 2000). The device switching time can be estimated as $t_R \simeq 4(\Delta V_{VP}/\Delta J_{PV})C_V$, where C_V is the device capacitance per unit area ($C_V \approx \varepsilon / W_{dep}(V)$). For the devices tested the expected modulation bandwidth was superior to 30 GHz (Figueiredo, 2000).

Following the frequency characterization, the waveguide low frequency electro-absorption response was characterized with no applied voltage, dc biased at slightly below the peak voltage, and on the valley region; the device was not dc biased in the NDC region in order to avoid self-oscillations. Light from a Tunics diode laser, tunable in the wavelength range 1480 nm to 1580 nm was fibre coupled to the waveguide, with the light output fibre coupled to an optical power meter or a high bandwidth photo-detector. The InGaAlAs/InP RTD-EAM waveguide transmission spectrum change due to the Franz-Keldysh effect absorption bandedge broadening induced by peak-to-valley switching is indicated in Fig. 15(a). The measured wavelength band-edge shift was 43 nm, which compares quite well with the estimation of 46 nm, equation 12. The low frequency electro-absorption response showed 5

dB absorption changes induced by 1 mV dc voltage increments, an exceptionally high transmission change per unit of voltage (Figueiredo, 2000). Figure 15(b) shows modulator response as function of the dc bias voltage when driven by 3 GHz voltage signals of amplitude from 1 mV to 100 mV; also represented is the RTD-EAM dc I –V characteristic. The rf photo-detected power increased by about 15 dB when the device dc bias point moved from the peak to the valley region at driving amplitudes as low as 50 mV. An indication the modulator can be driven by very low voltage signals due to its intrinsic built-in electrical amplifier.

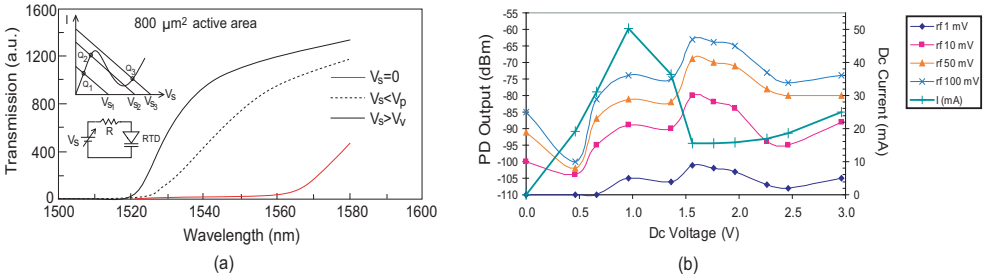

Fig. 15. (a) InGaAlAs RTD-EAM transmission spectrum in the wavelength range 1500 nm to 1580 nm, with the applied voltage as a parameter. (b) Modulator response as function of the dc bias voltage when driven by 3 GHz rf signals, with injected amplitude as a parameter.

RTD-EAM high frequency optical characterisation employed a microwave synthesized signal generator with a maximum output of +20 dBm and an upper frequency limit of 26 GHz (Figueiredo, 2000). Figure 16(a) shows the modulation depth as function of the light wavelength induced by the transition between the two PDC regions produced by a square signal with peak-to-peak voltage slight higher than $\Delta V_{VP} \sim 0.8$ V. The devices were dc biased in the valley region in order to minimize thermal effects and avoid self-oscillations. Modulation depths up to 28 dB were measured on devices with active areas around 800 μm², more than 10 dB superior to the values observed on the AlGaAs/GaAs devices. The modulator response up to 26 GHz driving signals for two power values is shown in Fig. 16(b).

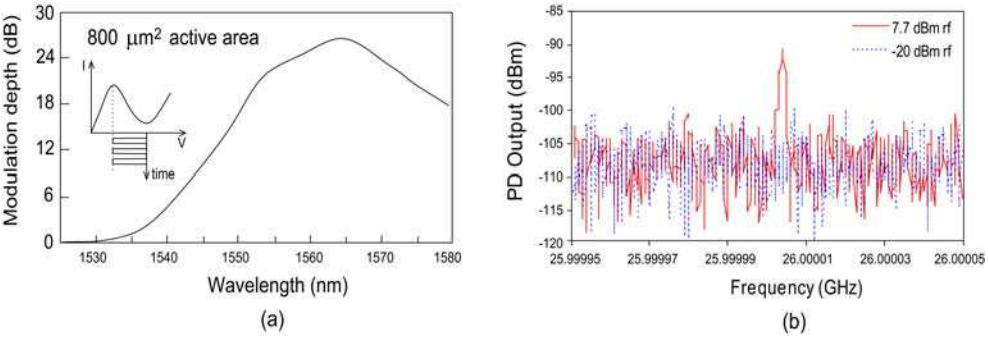

Fig. 16. (a) Modulation depth as function of the wavelength. (b) Spectrum of the 26 GHz photo-detected signal at the modulator driving power of -20 dBm and +7.7 dBm.